Cathodoluminescence of cerium dioxide: Combined effects of the electron beam energy and sample temperature

Jean-Marc Costantini, Pooreun Seo, Kazuhiro Yasuda, Akm Saiful Islam Bhuian, Tatsuhiko Ogawa, Didier Gourier

Version of Record: https://www.sciencedirect.com/science/article/pii/S0022231320303719
Manuscript_bf9d9662c0641a4c805337734bcc7cce

CATHODOLUMINESCENCE OF CERIUM DIOXIDE: COMBINED EFFECTS OF THE ELECTRON BEAM ENERGY AND SAMPLE TEMPERATURE

Jean-Marc COSTANTINI[1],

DEN-SERVICE DE RECHERCHES METALLURGIQUES APPLIQUEES, CEA, UNIVERSITE PARIS-SACLAY, 91191, GIF-SUR YVETTE CEDEX, FRANCE

Pooreun SEO, Kazuhiro YASUDA,

DEPARTMENT OF APPLIED QUANTUM PHYSICS AND NUCLEAR ENGINEERING, KYUSHU UNIVERSITY, 744 MOTOOKA, NISHI-KU, FUKUOKA, 819-0395 JAPAN

AKM Saiful Islam BHUIAN,

DEPARTMENT OF APPLIED QUANTUM PHYSICS AND NUCLEAR ENGINEERING, KYUSHU UNIVERSITY, 744 MOTOOKA, NISHI-KU, FUKUOKA, 819-0395 JAPAN; ATOMIC ENERGY CENTRE, CHATTOGRAM, BANGLADESH ATOMIC ENERGY COMMISSION, CHATTOGRAM - 4209, BANGLADESH

Tatsuhiko OGAWA,

NUCLEAR SCIENCE AND ENGINEERING CENTER, JAPAN ATOMIC ENERGY AGENCY (JAEA), SHIRAKATA 2-4, TOKAI, IBARAKI 319-1195, JAPAN

and Didier GOURIER,

CHIMIE PARIS-TECH, PSL UNIVERSITY, INSTITUT DE RECHERCHE DE CHIMIE-PARIS, 11 RUE PIERRE ET MARIE CURIE, 75005, PARIS, FRANCE

[1] Corresponding author's email : jean-marc.costantini@cea.fr

ABSTRACT

In-situ cathodoluminescence (CL) spectroscopy is used to study point-defect formation in cerium dioxide (CeO_2) by high-energy electrons (400 keV-1,250 keV) at ~100 K, 200 K, and 300 K in a high-voltage electron microscope (HVEM). Complementary CL spectra are also obtained for 20-keV electron excitation at ~300 K in a scanning electron microscope (SEM). Experiments were carried out on a single crystal and polycrystalline sintered sample. The more prominent and broad emission band centered at a photon energy of ~4.2 eV is ascribed to F^+ centers (oxygen vacancies) produced by the high-energy electron irradiation. Two other weaker CL bands centered at ~ 2.3-2.4 eV and 2.8-2.9 eV at 300 K are related to trivalent cerium ions, corresponding to 5d $\rightarrow$ 4f radiative transitions, regardless of electron energy. Similar spectra are recorded at 100 K and 200 K, yet with shifts and broadening of the latter emission bands. A maximum of all CL bands is found at ~600 keV electron energy for the polycrystalline sample regardless of temperature, and for the single crystal at 300 K. In contrast, a continuous increase versus electron energy is observed for the 4.2-eV band of the single crystal at 100 K and 200 K above a threshold corresponding to the oxygen displacement energy. The dependence of CL intensities on the primary electron energy is analyzed on the basis of the interplay of the luminescence cross section and oxygen displacement cross section. The electron energy dependence of ionization cross sections is addressed by relying on secondary electron spectra computed with the PHITS code which is benchmarked against other computer codes such as PENELOPE, as implemented in Geant4. The F^+ center band intensity is strongly reduced in the polycrystalline sample with respect to the single crystal in the same irradiation conditions regardless of temperature due to grain boundaries.

KEYWORDS: CATHODOLUMINESCENCE; CERIUM DIOXIDE; F CENTERS; SECONDARY ELECTRONS.

PACS CODES: 78.60.HK ; 61.72.JN ; 77.84.BW ; 79.20.HX

I) INTRODUCTION

The knowledge of the ballistic damage induced in mixed (U, Pu)O_{2-x} oxides under fast neutron irradiation is a key issue for modeling the long-term in-pile evolution of MOX nuclear fuels [1]. For this purpose, benchmark of molecular dynamics (MD) simulations of displacement cascades by experimental data on point-defect formation is of great interest on practical and fundamental standpoints. Electron-irradiation experiments provide data on point defects produced by elastic collisions at dilute concentrations that can help understanding the more complex case of the dense atomic collision cascades induced by fast neutrons. In this respect, cerium dioxide (CeO_{2-x}) or ceria can be envisioned as a non-radioactive surrogate of plutonium dioxide (PuO_{2-x}) [2]. The 5f and 4f electrons are localized for both Ce and Pu atoms, respectively, and the 3+ and 4+ oxidation states are actually present in both sub-stoichiometric oxides.

Point-defect formation by elastic collisions upon electron irradiation was studied by using *in-situ* cathodoluminescence (CL) spectroscopy in a high-voltage electron microscope (HVEM) [3]. Usually, such CL spectra are recorded for low energy electrons ($\leq$ 40 keV) to study native defects and impurities in insulators [4-7] or semiconductors [8-13] in a scanning electron microscope (SEM). Results have been recently obtained in a HVEM on several oxide systems for which emission bands of F centers (oxygen vacancies) with different charge states were recorded for high electron energies inducing oxygen recoils above the threshold displacement energy [14-15]. These *in-situ* experiments allowed following the in-beam processes of defect formation and recombination in these ceramics, for various temperatures and electron energies, before any off-beam thermally-activated annealing or ageing processes could occur. This knowledge is useful for the benchmark of MD simulations at short time scales compatible with the life times of excited states of luminescent defect species.

Regarding ceria, among several experimental techniques, such as transmission electron microscopy (TEM) [16-17], scanning transmission electron microscopy (STEM) [18], and various spectroscopies, such as electron paramagnetic resonance (EPR) spectroscopy [19] and UV-visible absorption or reflection spectroscopy [14, 20], were applied to study the point defects produced

after electron or ion irradiations. These results have revealed the formation of Ce^{3+} ions after irradiation. Moreover, photoluminescence (PL) spectroscopy was also currently used for studying native defects in pristine CeO_{2-x}, such as oxygen vacancies and Ce^{3+} ions [21-23]. All of these techniques usually give insight on the steady-state behavior of the virgin or irradiated material.

In contrast, *in-situ* CL experiments in the HVEM can in principle yield information on the instant point-defect formation under out-of-equilibrium conditions upon high-energy electron irradiation. The effect of electron energy can also be investigated by varying acceleration voltage of the microscope. For this purpose, experiments were thus conducted on a ceria single crystal and polycrystalline sintered sample. The CL spectra give evidence of a broad 4.2-eV band that can be assigned to F^+-centers for electron energies larger than or equal to 400 keV, whereas such a band is not recorded for 20-keV electrons in a SEM. A maximum of this CL signal is observed at ~600 keV for both kinds of samples at 300 K. The characteristic luminescence bands of Ce^{3+} ions are also recorded regardless of electron energy, with a similar maximum as a function of electron energy at 300 K. The CL band of F^+-centers show evidence of thermal quenching effects at 100 K and 200 K.

II) EXPERIMENTAL PROCEDURES

A half-disk of ceria polycrystalline sample in diameter of 3 mm and thickness of 150 µm, and with grain sizes of ~5 µm, was prepared by a sintering process at 1500°C for 24 hours. One side was polished by diamond suspension with a particle size of 1 µm, followed by the chemical polishing with a SiO_2 colloidal solution (particle size of 0.1 µm). The sample was confirmed to have a fine and flat surface by using a Nomarsky-type differential interference optical microscope. A small bulk single crystal (in thickness of about 0.5 mm) grown from a Li_2O-2 WO_3-based flux was also used.

The HVEM (JEM 1300NEF) of the Ultramicroscopy Research Center (Kyushu University, Fukuoka, Japan) is currently operated at electron energies between 400 keV and 1,250 keV. The beam current density can be varied by changing the intensity of the condenser lens. A beam intensity of 30 pA and flux of 3.8×10^{21} m^{-2} s^{-1} were used for an electron beam diameter of 30 µm. Some spectra

were collected for beam intensities up to 60 pA. The sample holder is equipped with a liquid-nitrogen cooling stage for temperatures down to ~100 K, preventing excessive in-beam heating of samples and temperature control and regulation.

The light emitted from samples was collected with an optical fiber probe (with a 600 µm core diameter and copper coating) designed for high throughput in the 180-1200 nm wavelength range and oriented at 46° off-beam. CL spectra in the 200-950 nm wavelength range were recorded with a Czerny-Turner HAMAMATSU MCA spectrometer (PMA-12 C10027-1) equipped with a cooled CCD linear image sensor (1024 channels). The wavelength resolution of the spectrometer was ~2 nm. Each spectrum was generally taken in 30 s under electron beam. Several spectra were recorded 5 times to check for the reproducibility of data. More experimental details can be found in previous papers [14-15]. Irradiation features such as the total inelastic stopping power ($(-dE/dx)_{inel}$) and range of electrons computed with the ESTAR code in the continuous slowing down approximation (CSDA) [24] are displayed in Table I.

The CL Spectra of both kinds of samples were recorded for a similar electron flux and fluence at ~100 K, 200 K, and 300 K, and for electron energies ranging from 400 keV to 1,250 keV. CL spectra were also recorded at ~300 K in a SEM for an accelerating voltage of 20 kV.

III) RESULTS

The as-recorded CL spectra of the single crystal and polycrystalline sample at 300 K are shown versus photon energy for the low (Fig. 1) and high electron energies (Figs 2 a-b). Gaussian profiles are used to fit these spectra with emission bands centered at ~1.7, 2.3-2.4, 2.8-2.9, 3.2, and 4.2 eV, for the high electron energies, and at ~2.4, and 2.8 eV, for the 20-keV electrons. The CL spectra at 100 K and 200 K exhibit broader emission bands that may be fitted with Gaussian profiles centered at photon energies of ~1.7, 2.0-2.6, 2.9-3.0, 3.2, and 4.2 eV (Figs. 2 c-d). No significant shifts of band centers (< 0.05 eV) are found versus electron energy for both samples. A very weak band of single crystal was seen to grow at ~3 eV for beam intensities larger than to 30 pA up to 60 pA at 800

keV. The band centers and corresponding full widths at half maximum (FWHM) deduced from standard deviations are reported in Table II. The intensity of the 4.2 eV band for the polycrystalline sample is about one order of magnitude smaller than that of the single crystal recorded in the same conditions (Figs. 2 b-d). For all samples, the sharp and most intense unresolved $R_{1,2}$ lines of Cr^{3+} impurities are detected at ~1.78 eV.

The dependence of CL integrated intensities (I_{CL}) at 300 K against electron energy is shown for both kinds of samples with error bars corresponding to $\pm 2\sqrt{I_{CL}}$ with 95% confidence on data (Fig. 3a). A clear maximum in CL signal is found at ~600 keV electron energy for the 4.2-eV band of the single crystal and for the 2.3-eV band of the sintered sample. A similar behavior is obtained for emission bands of the polycrystalline sample at 100 K and 200 K, but with a more sluggish dependence (Figs. 3b-c). In contrast, a continuous growth of the 4.2-eV band is found for the single crystal at 100 K and 200 K. Such results were double-checked by separate sets of measurements.

IV) DISCUSSION

The light emission process of CL upon electron bombardment of solids (so-called cathode rays) [25] differs from the classical photo-excitation process of photoluminescence (PL) [26]. It is generally admitted that the CL signal in semiconductors is proportional to the volume density of excess minority carriers [9, 10, 12]. Alternatively, excitation of CL spectra in oxides originate from the secondary electrons (and holes) generated by elastic and inelastic collisions induced by electron irradiation [15]. The CL signal is produced during trapping of these thermalized secondary electrons by electronic levels of defects and impurities in the band gap of the insulating oxide [4-5]. It is important to note that CL is not due to the fast primary electrons which are mostly transmitted through the targets, as indicated by simulations by the ESTAR code (Table I).

A more precise approach is based on the production of an electron-hole plasma by over band gap excitation (with a scaling of the valence plasma frequency (ω_p) on the band-gap energy [27], and subsequent damping and decay of the bulk plasmons into electron-hole pairs or excitons at very

short time scales of ~$1/\omega_p$ [25, 28]. The plasmon energy ($\hbar\omega_p$) and momentum ($\hbar q$) are transferred to the electron-hole pair in this process [29]. In semiconductors the thermalization of hot photo-excited electron-hole pairs at first takes place by electron-electron scattering during 10 fs to 100 fs, then by electron-phonon scattering during 100 fs to 1 ps [30-31]. The luminescent centers (so-called activators) can be excited either by direct interactions with plasmons or indirect interactions with free electrons and (or) holes [25]. However, the distinction between single particle and collective excitations is somewhat fictitious for insulators [28]. Moreover, the free carrier mobility is greatly restrained in wide band gap insulators such as ceria, as electrons and holes become very quickly trapped onto defects and activators, or self-trapped as polarons in a dielectric material [29, 32]. Therefore, we can neglect the ambipolar diffusion of excess carriers unlike for semiconductors [10-12]. Moreover, the drift in the internal electric field [32] is not taken into account, as a first approximation.

We assume in the following that the so-called "extrinsic" CL [8] results from electronic excitation and radiative decay of the defect and impurity levels populated by the thermalized secondary electrons, as discussed previously [15]. At 300 K, most shallow levels created by impurities and defects are fully ionized while deep levels created by charged point defects are partially filled. The cross section of the CL process (σ_{CL}) can be written as the product of the cross sections corresponding to the four following sequential and independent steps: i) ionization (σ_i), ii) electron/hole trapping (σ_t), iii) electronic excitation (σ_e), and iv) radiative decay (σ_r). Trapping of thermalized carriers may also occur directly on excited states rather than on the ground state of the defect levels. In that case, the CL process is reduced to three steps only. Thermal quenching by phonon-assisted non-radiative channels reduces the CL yield at high temperature [8, 10], just like for PL [26].

The temperature dependence of the CL intensity was previously addressed by considering the opposite effects on σ_t and σ_r: σ_t increases with temperature, whereas σ_r decreases [15]. Either a maximum or a steady increase versus temperature was found depending on these respective effects.

The temperature effect on the various cross sections is summarized in Table III. Moreover, no significant defect annealing and thermal diffusion are expected up to 300 K for refractory oxides, unlike for most metals [33]. The contribution to quenching by other non-radiative channels due to defects and impurities is a challenging issue even though it is very difficult to assess [10].

Note that emission by direct bound-exciton radiative recombination from the defect or impurity levels can be overlooked, since it is only effective at low temperature (< 100 K) and quenched at higher temperature for a doped wide band gap semiconductor [34]. The CL of self-trapped excitons in MgF_2 (with the fluorite structure) is also thermally quenched at temperatures above 55 K [35]. The exciton radiative recombination across the band gap (so called "intrinsic" CL [8]) is usually quenched at such high temperature. Actually, no emission is recorded in the present CL spectra for the band gap energy of ~5.5-6eV deduced by electron energy loss spectroscopy (EELS) [36-37]. More details on this analysis are provided in a previous paper [15].

IV.1) Analysis of CL spectra

The main emission bands observed in this work are centered at photon energies of ~1.7 eV, 2-2.5 eV, ~3 eV and ~4 eV. To interpret these CL bands, it is useful to give a brief survey of literature on PL data in CeO_2, which seem to show divergent interpretations as the same bands were attributed either to F-type centers (oxygen vacancies, V_O) or to 5d-4f transitions of Ce^{3+}. For example, Aškrabič et al. assigned the 1.7-eV band and the 2-2.5 eV to charge transfer (CT) transitions from F^+ centers ($V_O^{\cdot}$) to the oxygen 2p states and to F^0 centers (V_O^x) and F^+ centers, respectively [22]. Alternatively the same bands at 2-2.5 eV were associated to $5d^1 \rightarrow 4f^1$ transitions of Ce^{3+} ions in non-stoichiometric nano-crystalline ceria (nc-CeO_2) by Maksimchuk et al. [23]. Generally, PL bands at ~2 eV are attributed to Ce^{3+} luminescence, for example in the case of YAG: Ce^{3+} [38] and ZrO_2: Ce^{3+} [39]. Finally, the bands at 3.1-3.15 eV were ascribed by Morshed et al. to 4f → 2p charge transfer (CT) transitions for CeO_2 films on a silicon substrate [21] and nc-CeO_2 [23]. Also, the band at 2.9-3.0 eV was also assigned by Aškrabič et al. to CT transitions from the F^{2+} center ($V_O^{\cdot\cdot}$) level to Ce^{3+} ($4f^1$) for nc-CeO_2

[22]. The emission band at 3.18 eV in $Lu_2SiO_5:Ce^{3+}$ (LSO: Ce^{3+}) was attributed to Ce^{3+} in Lu site by Suzuki et al. [40], while *ab initio* calculations in this compound [41] for LSO: Ce^{3+} showed that the emission of Ce^{3+} in a crystallographic site occurs at higher photon energy (~ 3.2 eV) than that of a Ce^{3+} adjacent to an oxygen vacancy (~ 2.6 eV). Note that the luminescence of Ce^{3+} ions is quenched in some oxide hosts such as La_2O_3 [42] and Lu_2O_3 [43].

This variety of interpretations of emission bands may appear somewhat confusing. However they are not totally contradictory if we consider the CeO_2 structure and more precisely a pair of Ce^{4+} ions connected by two lattice O^{2-} ions (Fig. 4a). Let us consider a neutral oxygen vacancy (V_O^x) at one oxygen site connecting the two cerium ions schematized as a Ce^{4+}-V_O^x-Ce^{4+} cluster (where the other connecting O^{2-} ion is omitted for clarity). First principle calculations showed that the two electrons of V_O^x are mostly localized on the two neighboring Ce^{4+} ions, forming a Ce^{3+}-$V_O^{\cdot\cdot}$-Ce^{3+} cluster in which more than 0.9 electrons are localized on each Ce and about 0.1 electron remains on the vacancy site [44]. Moreover, other *ab-initio* DFT calculations have shown that such trimer clusters are dominant defects for low oxygen potential, such as for small oxygen deficiency and under vacuum conditions [45]. Despite this partial electron delocalization, the large electron density at cerium sites favors the interpretation of CL data in terms of Ce^{3+} optical transitions rather than V_O-type (or F-type in spectroscopic notation) transitions. This interpretation of CL bands is confirmed by EPR data. Although Aškrabič et al. [22] ascribed to F^+ centers the weak EPR transitions at g = 1.96 and g = 1.94, this weak signal is due to Cr^{3+} impurities, as demonstrated by Figaj and Becker [46]. If present, the EPR of diluted Ce^{3+}, even in a symmetrical environment, would be too much anisotropic to be observable in powder samples. It would be eventually detected only for high concentrations of Ce^{3+}. However, the EPR signal of Ce^{3+} has been clearly observed in electron-irradiated CeO_2 single crystals [19]. As expected, it is more anisotropic with g-factors ranging between 1.1 and 1.43, and it can be observed only because single crystals can be oriented in the external magnetic field, in contrast to powder samples.

Therefore, instead of using a classical description of oxygen vacancies in terms of F, F^+ and F^{2+} centers, we consider the different possible electronic configurations of the neutral oxygen vacancy V_O^x, written in terms of a Ce^{4+}-V_O^x-Ce^{4+} cluster. Assuming the electro-neutrality, we may consider three different electronic configurations for this cluster, leading to two or three types of Ce^{3+} ions (Fig. 4a): (i) configuration Ce^{3+}-$V_O^{\cdot\cdot}$-Ce^{3+} with two neighboring Ce^{3+} ions, (ii) configuration Ce^{3+}-$V_O^{\cdot\cdot}$-Ce^{4+} with the other electron trapped in the form of a Ce^{3+} at undistorted substitution position located at a larger distance from the vacancy, and (iii) configuration Ce^{4+}-$V_O^{\cdot\cdot}$-Ce^{4+} with the two electrons trapped at two undistorted Ce^{3+} sites at a larger distance from the vacancy. In terms of classical oxygen vacancy centers F, F^+ and F^{2+}, i.e. not considering the electron localization on a Ce adjacent to the vacancy, configurations (i), (ii) and (iii) correspond to the F center (V_O^x), F^+ center ($V_O^{\cdot}$) and F^{2+} center ($V_O^{\cdot\cdot}$), respectively. In configurations (i) and (ii), EPR and CL detect only the Ce^{3+} ions where the compensating electrons are trapped. In the case of configuration (iii), EPR detects Ce^{3+} as in (i) and (ii), but CL contains both the emission of Ce^{3+} and of a classical F^+ center, as discussed below.

The fitting of CL spectra at 300 K regardless of primary electron energies (Figs. 1-2) yields two broad emission bands centered at 2.3-2.4 eV and 2.8-3.0 eV with FWHM of ~0.5 eV, that are more intense in the polycrystalline sample than in the single crystal. According to the above considerations, those two CL bands arise from spin and parity-allowed $5d^1 \rightarrow 4f^1$ electric-dipole transitions with large oscillator strengths. The $4f^1$ (^2F) level of Ce^{3+} is split into $^2F_{5/2}$ and $^2F_{7/2}$ sub-levels by the spin-orbit coupling interaction, with an energy difference of ~0.25 eV (~2,000 cm^{-1}) [47-51]. It might be tempting to attribute the two prominent CL bands to the two $5d^1 \rightarrow 4f^1$ ($^2F_{7/2}$, $^2F_{5/2}$) transitions. However, there are several arguments against this interpretation. In the case of the polycrystalline sample: a) the splitting of 0.5 eV at 300 K to 0.9 eV at 100 K between these bands is larger than the theoretical value 0.25 eV for the spin-orbit splitting of Ce^{3+}; b) the observed splitting

increases from 0.5 to 0.9 eV, whereas the spin-orbit coupling should be independent of temperature; c) the low energy CL band shifts to lower temperature (2.3 to 2.0 eV) upon decreasing the temperature from 300K to 100 K; d) the intensities of the two transitions differ by a factor ~5 (~1.5 for the single crystal).

Consequently we must attribute these two CL bands to two different types of emitting Ce^{3+} centers, hereafter referred to as Ce_I (2.8 – 3.0 eV) and Ce_{II} (2.2 – 2.3 eV). By comparison with experimental and theoretical analyses of emission bands in LSO: Ce^{3+} [41], the CL band Ce_I may be attributed to a Ce^{3+} at unperturbed crystallographic site of CeO_2, and the CL band Ce_{II} to a Ce^{3+} adjacent to an oxygen vacancy. Two features of these CL bands argue in favor of this interpretation: a) Examination of CL spectra of the polycrystalline sample at 100 K indicates that the band around 3 eV might be composed of two components separated by about 0.25 eV, corresponding to the spin-orbit splitting of Ce^{3+} (Fig. 2d, marked with arrows); b) The low energy CL band (around 2 eV) shows a temperature quenching effect as it is weaker at 300 K than at 100 K (Fig. 2 b, d). These two features (the spin-orbit splitting and the selective temperature quenching) were also observed in LSO: Ce^{3+} [41] for Ce^{3+} in undistorted crystallographic site and for a Ce^{3+} adjacent to an oxygen vacancy, respectively. The schematic energy levels of Ce_I and Ce_{II} centers are given in Fig. 4b, assuming a 5.5 – 6 eV energy difference between the conduction band (Ce-5d) and the valence band (O-2p) [36, 37, 52, 53]. The Ce_I center (2.8-3.0 eV emission band), attributed to Ce^{3+} at undistorted crystallographic site, are found in configurations (ii) and (iii) of the oxygen vacancy in Fig. 4a, while the Ce_{II} center (2.0 – 2.4 eV emission band), attributed to a Ce^{3+} adjacent to an oxygen vacancy, corresponds to configurations (i) and (ii) of the oxygen vacancy.

Additional CL bands are also observed after electron irradiation, which are absent for low energy electron irradiation (20 keV, Fig. 1). The broad 4.2-eV band is more intense in the single crystal (Fig. 2a, c) than in the polycrystalline sample (Fig. 2b, d). It is also represented in Fig. 5 for the CL spectrum of the single crystal irradiated at the electron energy of 1,250 keV. Similar CL bands centered at 3.8 eV and 4.1 eV were previously assigned to F^+ centers for sapphire (α-Al_2O_3) and

yttria-stabilized zirconia (ZrO_2: Y), or YSZ, respectively [14-15]. Within the schematic model for the oxygen vacancy in Fig. 4, the 4.2 eV band could correspond to the situation of configuration (iii) (Fig. 4a) in which the vacancy corresponds to a F^{2+} center ($V_O^{\cdot\cdot}$), with two neighboring Ce^{4+} ions. Consequently this center has no Ce^{3+} character, and the 4.2 eV band could result from the electron capture by the vacancy (the Ce^{4+}- $V_O^{\cdot\cdot}$ - Ce^{4+} cluster), giving an F^+ center emission, as schematized in Fig. 4c. Just before the emission, the captured electron is localized in the middle of this symmetric cluster, i. e. on the oxygen vacancy site (this corresponds to an excited F^+ center). According to the Frank-Condon principle, the electron is still localized at the V_O site during the emission (vertical transition in a configuration coordinate model). This final state corresponds to an unrelaxed (transient) state of the F^+ ground state. Immediately after the emission, the electron is then shifted to one of the two Ce^{4+}, giving a Ce^{3+}-$V_O^{\cdot\cdot}$- Ce^{4+} cluster. This center corresponds to the relaxed state of the F^+ center (Fig. 4c). This CL emission at 4.2 eV can be summarized by the following three-step reaction:

Ce^{4+}- $V_O^{\cdot\cdot}$ - Ce^{4+} + e^- $\rightarrow$ [Ce^{4+}- $V_O^{\cdot}$ - Ce^{4+}]* $\rightarrow$ [Ce^{4+}- $V_O^{\cdot}$ - Ce^{4+}] + hν (4.2 eV) $\rightarrow$ [Ce^{3+}- $V_O^{\cdot\cdot}$ - Ce^{4+}] (EPR)

Almost all of CL bands have a FWHM of about 0.5 eV, except for the 4.2-eV band having a width of ~1 eV as the other F^+ centers in sapphire and YSZ [7, 14, 15, 54]. The assignment of the CL bands is summarized in Fig. 5 and Table II.

It is important to note that EPR indicated only the formation of Ce^{3+} centers after electron irradiation, and not F^+ center as previously thought [19], whereas CL contains an F^+ emission at 4.2 eV. This contradictory result is due to the fact that EPR spectra are recorded after irradiation, while CL spectra are recorded during irradiation. This implies that the classical F^+ center ground state has a short lifetime and exists only during the F^+ emission. Just after the F^+ emission, the electron is transferred from the oxygen vacancy to a neighboring Ce^{4+} ion, giving a Ce^{3+}-$V_O^{\cdot\cdot}$ - Ce^{4+} center (Fig. 4c). This model implies that the ground state of the Ce^{3+}- $V_O^{\cdot\cdot}$ - Ce^{4+} center (Ce_{II}) is at lower energy

than the F^+ ground state, which lies by construction at ~1.8 eV above the top of the valence band (Fig. 4b). First principle calculations indicate that the ground state of the Ce^{3+}- $V_O^{\cdot\cdot}$ - Ce^{4+} center in CeO_2 is at ~1.4 eV from the valence band [44], i.e. ~0.4 eV below the F^+ ground state, which agrees with our interpretation. A schematic energy level diagram corresponding to the different CL bands is proposed in Fig. 4b.

It is also important to note that this 4.2 eV CL band is missing in samples (single crystal and polycrystal) irradiated with 20-keV electrons (Fig.1). This can be explained by considering the displacement cross sections computed for oxygen atoms [55] with the SMOTT/POLY code [56] devised for polyatomic targets. These calculations take into account the primary electron-nucleus collisions and small atomic displacement cascade contribution, and the admitted value of threshold displacement energy of $E_d(O)$ = 35 eV based on the upper boundary value (33 eV) deduced from experiments at the HVEM [57]. Note that molecular dynamics simulations gave smaller values of 27 eV [58], and 20 to 35 eV [59]. A larger value of $E_d(Ce)$ = 58 eV is admitted for cerium [57]. Our data show that oxygen displacement by elastic electron-nucleus collisions can only occur for electron energies higher than ~200 keV [55]. This explains the lack of 4.2 eV CL band in CeO_2 irradiated by 20 keV electrons (Fig.1). However it must be noticed that the Ce_I (~2.8-2.9 eV) and Ce_{II} (~2.3 eV) CL bands are present even after 20 keV electron irradiation, and may originate from two possible processes: (a) excitation of Ce^{3+} at lattice position (Ce_I) and Ce^{3+} adjacent to preexisting oxygen vacancies (Ce_{II}), and (b) the production of oxygen vacancies in configurations (i) and (ii) by electronic excitations. Hypothesis (b) is not totally unlikely as the inelastic stopping power $(-dE/dx)_{inel}$ is 4 to 6 times larger for 20-keV electrons than for 400 keV to 1,250 keV, where it is nearly constant (Table I).

Comparison of CL spectra of the sintered sample (Figs. 2 b, d) and the single crystal (Figs. 2a, c) shows that the 4.2-eV band is much weaker in the former than in the latter regardless of temperature, whereas the signal of Ce^{3+} ions is larger in intensity, even though the sintered sample is thinner. This effect cannot derive from defect diffusion to the grain boundaries of the sintered sample, as may be expected, owing to the short lifetime of the excited state and low temperatures. It

might rather be related to athermal non-radiative channels due to impurities [10, 26] segregated at grain boundaries. Emission lines of these impurities may not be seen due to thermal quenching at 100 K and higher temperature. Prompt recombination/annihilation of oxygen Frenkel pairs at grain boundaries may also contribute to such a decrease.

Finally, the rather broad CL band at 1.7 eV (FWHM = 0.4 eV) observed for high energy electron irradiation (Fig. 2) was already encountered for other oxide systems with different band gap energies [14-15], and is likely related to a 3d-transition element impurity such as Ti^{3+} in sapphire [4-5]. The very narrow peaks inside this 1.7 eV band are due to $^2E - {}^4A_2$ emission bands ($R_{1,2}$ lines) of Cr^{3+} impurities in oxide hosts [60].

IV.2) Effect of electron energy

In the case of semiconductors, the effect of electron energy was previously addressed for low-energy electron excitations ($E \leq 40$ keV) of n-doped GaAs in a SEM [9, 12], where diffusion and recombination processes at the surface of excess free minority carriers were considered to model the electron-energy dependence of the CL signal. A maximum arises from the depth dependence of the light emission yield caused by self-absorption. The maximum shifts to a higher voltage when the surface recombination is dominant [12]. However, in the present study on CeO_2, the primary electrons are shot through the targets and the secondary electron distribution can be considered as homogeneous across the sample thickness regardless of the primary electron energy [15]. The maximum in CL intensity (Fig. 3) cannot derive from inhomogeneity of the depth profile of secondary electrons and drift of excess carriers to the insulator surface, unlike for low-energy electron irradiation of semiconductors [9].

In order to analyze the effect of electron energy (E) for ceria, the secondary electron spectra were computed with the PHITS computer code [61], as was done previously for sapphire and YSZ [15]. The output of these Monte Carlo (MC) simulations is the double differential ionization cross section ($d^2\sigma_i/dE_s d\Omega$) including the elastic and inelastic electron-electron collisions per steps of

secondary electron energy (E_s) and solid angle (Ω) for Ce and O atoms, computed for a thin target (10 µm). This is shown for forward collisions at scattering angles of $0° \leq \theta \leq 18°$ with a maximum E_s value equal to E for head-on collisions (Fig. 6). Electron-nucleus scattering is also included for the high-energy events.

The electronic cascade is followed for kinetic energies of secondary electrons down to 1 keV, which is the lower boundary of the PHITS code. For secondary electrons, it takes a time of ~100 fs on average to reach 1 keV. The number of secondary electrons produced inside the 150-µm thick sample during the scattering process down to 1 keV is computed versus primary electron energy (Fig. 7). Even though the inelastic electron stopping power is scarcely energy dependent for energies ranging from 400 keV to 1,250 keV (Table I) the number of electrons increases with the incident electron energy because electron-gamma cascade develops with increasing electron energy. The latter 1-keV electrons have a negligible range as compared to the sample thickness. Cooling of those hot 1-keV electrons to thermal energy was followed by MC simulations in a water medium with the RITRACKS computer code [62]. A cooling time of 37.8 ± 8.4 fs was found for 50 events.

Little deviations in cross sections were found at low E_s values for the various primary electron energies [15]. This corresponds to small differences in $(-dE/dx)_{inel}$ (Table I) which is mainly dominated by the contribution of low-energy secondary electrons [63]. Note that the maximum in CL intensity versus primary electron energy (Fig. 3) cannot be accounted for by the small variations in $(-dE/dx)_{inel}$ by only ~10% (Table I), as $(-dE/dx)_{inel}$ has its minimum value in this energy range. As a result, the number of electron-hole pairs generated inside the sample is about the same between 400 keV and 1,250 keV [64].

As was done before, a cut-off energy (E_{cut}) was used to select the range of efficient secondary electrons giving a maximum light emission yield: E_{cut} is the energy corresponding to an electron range equal to the sample thickness, as computed with the ESTAR computer code [24]. This value is obviously larger for the 0.5-mm thick single crystal (E_{cut} = 600 keV) than for the 150-µm thick sintered sample (E_{cut} = 250 keV) (Fig. 6). This rough approximation was confirmed by simulations of the

survival probability of secondary electrons inside a 150-μm thick YSZ target versus E_s for E = 400 keV and E = 1,250 keV, on the basis of spatial distributions of secondary electrons [15].

Although electron-electron scattering is dominated by forward collisions, there is actually a large contribution for θ ~90° after integration on Ω, even though ($d^2\sigma_i/dE_s d\Omega$) is lower [15]. The double differential cross sections for Ce atoms with a width of 18° are integrated over 2π sr. solid angle from the lower energy boundary of 1 keV to the maximum E_s value for a given primary electron energy. Simulations with the PHITS code are benchmarked against other computer codes such as PENELOPE [65] by checking the effect of the selection of cross sections. A rather good agreement on the integrated differential cross section ($d\sigma_i/d\theta$) is found between the various data banks as a function of θ for E = 400 keV and E = 1,250 keV (Fig. 8). The maximum ($d\sigma_i/d\theta$) values for θ ~0° and θ ~70° are almost equal, and no strong differences are found as a function of E, between 400 keV and 1,250 keV, in contrast to our previous discussion based on ($d^2\sigma_i/dE_s d\Omega$) for $E_s = E_{cut}$ (Fig. 6) [15]. To check the possible variation of the cross sections of electrons, the electron production cross section ($\sigma_{i,\,tot}$) integrated on θ was calculated by PHITS and Geant4 [66]. Three models as implemented in Geant4, the PENELOPE low-energy electron models [67-68], LIVERMORE, and EMX [69] were employed,. All of them exhibit a decrease by a factor ~20-30 % from 400 keV to 1,250 keV (Table IV). It should be noted that the cross sections are as large as a few 10,000 barns because they are attributed to electromagnetic interaction, whose range is infinite in principle, bound by in-medium screening. These values are consistent with the value of the evaluated electron cross section library . It should be also noted that the cross sections calculated by PHITS and PENELOPE tend to be higher than the others because they additionally include the electrons down-scattered by Bremsstrahlung and those from Auger-electron emission, respectively.

However, we surmise a stronger decrease of the excitation cross section (σ_e) versus primary electron energy. Such kind of decrease was indeed found for the “apparent cross section” (quote) for fluorescence of molecular levels of nitrogen N_2 (including primary and secondary electron contributions) upon electron irradiation up to 1 GeV above a maximum at low energy (< 100 eV) [70].

Such behavior can also apply to the case of secondary electron trapping on an excited state instead of the ground state of the defect level.

Moreover, the CL intensity (I_{CL}) for point defects produced by elastic collisions should increase with the displacement cross section (σ_d). As a result, we assume that I_{CL} writes:

$$I_{CL} = K \sigma_{CL} \sigma_d \quad (1)$$

where K stands for a constant including the factors related to the experimental set up and conditions . We assume that the cross-section for electron/hole trapping σ_d can be approximated as $(E - E_0)^{\beta}$, for $E \geq E_0$, where E_0 is the threshold electron energy for atomic displacement. However, it is liable to think that σ_t does not directly depend on E, but depends on temperature only, as an intrinsic feature of the defect electronic levels [15]. On the other hand, the radiative decay cross section (σ_r) decreases with E, since the luminescence can be quenched by increasing the point defect concentration [10, 26]. Therefore, we surmise a dependence of $E^{-\alpha}$ for the product of σ_r and the electronic excitation cross section σ_e. As a result, the dependence of I_{CL} on the primary electron energy writes as:

$$I_{CL} = K' E^{-\alpha} (E - E_0)^{\beta} \quad (2)$$

where K' is another constant. A strong decay versus E, i. e. a large α exponent, is required to counteract the steep increase of the total displacement per atom (dpa) induced inside a 150-µm thick sample by the primary electrons and the secondary electron cascade versus E (Fig. 7). Those dpa values derive from oxygen displacement only owing to the smaller E_d value for oxygen atoms (35 eV) with respect to cerium atoms (58 eV) [57]. The effect of primary electron energy on the various cross sections is summarized in Table III.

Such kind of function yields a maximum of I_{CL} versus E for both samples at 300 K (Fig. 3 a) whereas I_{CL} is expected to increase steadily if σ_d is only considered. A limiting factor must be included to account for this maximum. Least-square fits with Eq. (2) give values of E_0 and α and β exponents for the various bands (Table V). The value of E_0 ~400 keV for the F^+ center 4.2-eV band of the single crystal and polycrystalline sample at 300 K is rather consistent with the data of oxygen displacement by elastic electron-nucleus collisions (Fig. 7). The threshold E_0 value is comprised between 200 keV and 400 keV in agreement with the CL data. The α exponent (~2) is in agreement with previous results for F^+ center bands in sapphire and YSZ single crystals with values of ~3 [15]. A smaller exponent (~0.6) is deduced for the 4.2-eV band of the polycrystalline sample at 300 K (Table V). The behavior of CL bands assigned to luminescence of Ce^{3+} at 300 K is quite similar for both kinds of samples with α exponents of ~1.5 (Table V). Fitted parameters for the polycrystalline sample at 100 K and 200 K show similar consistent data versus electron energy. The behavior of CL bands related to Ce^{3+} luminescence at 300 K show that these ions are definitely produced with a similar threshold electron energy as the F^+ centers by charge compensation of the 2+ oxygen vacancies for the high-energy electrons. In contrast, the same CL bands for the 20-keV electron excitation likely derive from ionization effects [71].

However, such analysis is not relevant for F^+-center data of the single crystal at 100 K and 200 K not showing a maximum but rather a steady increase against electron energy above the threshold energy of E_0 ~400 keV (Figs. 3b-c). A linear extrapolation of the 100-K data yields an E_0 value of ~100 keV (Fig. 3c). It looks like Eq. (1) is reduced to the $(E - E_0)^\beta$ term corresponding to σ_d only. The increase of I_{CL} is roughly consistent with the increase of σ_d from 400 keV to 1,250 keV [55]. The fitted values for the three bands are given in Table V. The combination of an electron energy increase and a temperature decrease depends on the respective evolutions of σ_{CL} and σ_d: either a maximum or a continuous increase of I_{CL} can be obtained when lowering the sample temperature, as shown in Table III. This is similar to the temperature effect for a given electron energy yielding either a maximum or a continuous increase [15]. One must bear in mind, as explained above, that σ_r decays with

temperature due to thermal quenching [8, 10, 15, 26]. This means that the α exponent should depend on temperature, as found in the fits (Table V). This may explain the almost linear increase of I_{CL} for F^+ centers in the single crystal at 100 K and 200 K, whereas a maximum is found in the sintered sample, for different thermal quenching behavior of the luminescence.

V. CONCLUSIONS

The CL of cerium dioxide was studied for electron energies varying between 400 keV and 1,250 keV at ~100 K, 200 K, and 300 K in a HVEM and for 20-keV electrons at ~300 K in a SEM. A broad and most prominent CL band centered at photon energy of ~4.2 eV is recorded for the high-energy electrons only (above 200 keV), whereas smaller bands at ~2.3-2.6 eV and 2.8-3.0 eV are found for all electron energies. The 4.2 eV band is assigned to emission of F^+ centers produced by elastic electron-nucleus collisions above a threshold electron energy corresponding to the oxygen displacement energy. The lower energy CL bands are ascribed to Ce^{3+} ions induced by charge compensation of oxygen vacancies for the high-energy electrons, and by ionization effects for the 20-keV electron excitation having a higher inelastic stopping power. Similar spectra are obtained at 100 K and 200 K, yet with broader and slightly shifted emission bands. The F^+ CL signal is weaker for the polycrystalline sample compared to the single crystal in the same conditions regardless of temperature due to effects of grain boundaries. The dependence of CL integrated intensities as a function of the primary electron energy for both kinds of targets is interpreted by the interplay of the oxygen displacement cross section and the luminescence cross section. For this purpose, secondary electron spectra were computed with the PHITS code which is benchmarked against other computer codes such as PENELOPE and Geant4.

ACKNOWLEDGMENTS: The HVEM-CL experiments were performed at The Ultramicroscopy Research Center of Kyushu University supported as a HVEM-Project. This work was also supported by JSPS KAKENHI with a grant number of JP19K05333. Lynn Boatner (Oak Ridge National Laboratory, USA) is

greatly thanked for providing the ceria single crystal. The authors are also indebted to Davide Mancusi (CEA, Université Paris-Saclay, France) for his help in using the Geant4 computer code.

References

[1] R. Devanathan, L. Van Brutzel, A. Chartier, C. Gueneau, A. E. Mattsson, V. Tikare, T. Bartel, T. Besmann, M. Stane, and P. Van Uffelenf, Energy Environ. Sci., 3 (2010) 1406.

[2] W. J. Weber, Radiation Effects, 83 (1984) 145.

[3] K. Furumoto, T. Tanabe, N. Yamamoto, T. Daio, S. Matsumura, and K. Yasuda, Mater. Trans., 54 (2013) 854.

[4] P. Jonnard, C. Bonnelle, G. Blaise, G. Rémond, and C. Roques-Carmes, J. Appl. Phys. 88 (2000) 6413.

[5] M. Ghamnia, C. Jardin, and M. Bouslama, J. of Electr. Spectrosc. and Related Phenomena, 133 (2003) 55.

[6] D. Maestre, A. Cremades, and J. Piqueras, J. Appl. Phys., 95 (2004) 3027.

[7] G. Pezzoti, K. Wan, M. C. Munisso, and W. Zhu, Appl. Phys. Lett., 89 (2006) 041908.

[8] B. G. Yacobi, and D. B. Holt, J. Appl. Phys. 59 (1985) R1.

[9] W. Hegert, P. Reck, L. Pasemann, and J. Schreiber, Phys. Stat. Sol. (a), 101 (1987) 611.

[10] V. I. Petrov, Phys.-Uspekhi, 39 (1996) 807.

[11] A. Djemel, R. J. Tarento, J. Castaing, Y. Marfaing, and A. Noiri, Phys. Stat. Sol. (a), 168 (1998) 425.

[12] A. Djemel, A. Noiri, S. Kouissa, and R. J. Tarento, Phys. Stat. Sol. (a), 191 (2002) 223.

[13] H. Lei, H. S. Leipner, V. Bondarenko, and J. Schreiber. J. Phys. Condens. Matter, 16 (2004) 279.

[14] J. M. Costantini, Y. Watanabe, K. Yasuda, and M. Fasoli, J. Appl. Phys., 121 (2017) 153101.

[15] J.-M. Costantini, T. Ogawa, AKM S. I. Bhuian, K. Yasuda, J. Lumin. 208 (2019) 108.

[16] K. Yasunaga, K. Yasuda, S. Matsumura, and T. Sonoda, Nucl. Instr. and Meth. B, 250 (2006) 114.

[17] K. Yasuda, M. Etoh, K. Sawada, T. Yamamoto, K. Yasunaga, S. Matsumura, and N. Ishikawa, Nucl. Instr. and Meth., 314 (2013) 185.

[18] S. Takaki, K. Yasuda, T. Yamamoto, S. Matsumura, and N. Ishikawa, Nucl. Instr. and Meth. B, 326 (2014) 140.

[19] J.-M. Costantini, L. Binet, N. Touati, G. Lelong, M. Guillaumet, and W. J. Weber, J. Appl. Phys., 123 (2018) 025901.

[20] J.-M. Costantini, G. Gutierrez, H. Watanabe, K. Yasuda, S. Takaki, G. Lelong, M. Guillaumet, and W. J. Weber, Philos. Mag. 99 (2019) 1695.

[21] A. H. Morshed, M. E. Moussa, S. M. Bedair, R. Leonard, S. X. Liu, and N. El-Masry, Appl. Phys. Lett., 70 (1997) 1647.

[22] S. Askrabic, Z. D. Dohcevic-Mitrovic, V. D. Araujo, G. Ionita, M. M. de Lima Jr, and A. Cantarero, J. Phys. D: Appl. Phys., 46 (2013) 495306.

[23] P. O. Maksimchuk, V. V. Seminko, I. I. Bespalova, and A. A. Masalov, Functional Mater., 21 (2014) 3.

[24] "*Stopping Powers for Electrons and Positrons*", International Commission on Radiation Units and Measurements ICRU Report 37 (1984).https://physics.nist.gov/PhysRefData/Star/Text/method.html

[25] L. Ozawa, and M. Itoh, Chem. Rev., 103 (2003) 3835.

[26] D. Curie, "*Luminescence in Crystals"* (J. Wiley, New York, 1963).

[27] I. Egri, Solid State Commun., 44 (1982) 563.

[28] N. Itoh, and A.M. Stoneham, "*Materials Modification by Electronic Excitation*" (Cambridge University Press, Cambridge, 2000).

[29] H. Raether, "*Excitation of Plasmons and Interband Transitions by Electrons*", Springer Tracts in Physics, vol. 88 (Springer, Berlin, 1979) p.72.

[30] M. A. Rodriguez-Meza, and J. L. Carrillo, Rev. Mexic. De Fisica, 48 (2002) 52.

[31] P. Narang, R. Sundataraman, and H. A. Atwater, Nanophotonics, 5 (2016) 96.

[32] J. P. Ganachaud, and A. Mokrani, Surf. Sci., 334 (1995) 329.

[33] A. C. Damask and G. J. Dienes, "*Point Defects in Metals"* (Gordon and Breach, New York, 1971).

[34] M. D. Sturge, E. Cohen, and K. F. Rodgers, Phys. Rev. B, 15 (1977) 3169.

[35] V. N. Kolobanov, V. V. Mikhailin, S. P. Chernov , D. A. Spassky, V. N. Makhov, M. Kirm, E. Feldbach, and S. Vielhauer, J. Phys.: Condens. Matter, 21 (2009) 375501.

[36] E. Wuilloud, B. Delley, D. Schneider, and Y. Baer, Phys. Rev. Lett., 53 (1984) 202.

[37] E. Wuilloud, B. Delley, D. Schneider, and Y. Baer, J. Magn. Magn. Mater., 47-48 (1985) 197.

[38] V. Pankratov, L. Grigorjeva, D. Millers, T. Chudoba, R. Fedyk, and W. Lojkowski, Solid State Phenom., 128 (2007) 173.

[39] B. A. Danja, IOSR J. Appl. Chem., 9 (2016) 92.

[40] H. Suzuki, T. Tombrello, C. Melcher, J. Schweitzer, IEEE Trans. Nucl. Sci., 40 (1993) 380.

[41] Y. Jia, A. Miglio, M. Mikami, and X. Gonze, Phys. Rev. Mater., 2 (2018) 125202.

[42] G. Blasse, W. Schipper, and J. J. Hamelink, Inorg. Chim. Acta, 189 (1991) 77.

[43] W. M. Yen, M. Raukas, S. A. Basun, W. Van Schaik, and U. Happek, J. Lumin., 69 (1996) 287.

[44] X. Han, J. Lee, H-I. Yoo, Phys. Rev. B, 79 (2009) 100403.

[45] T. Zacherle, A. Schriever, R. A. de Souza, and M. Martin, Phys. Rev. B, 93 (2013) 134104.

[46] M. Figaj, and K. D Becker, Solid State Ionics, 141-142 (2001) 507.

[47] G. Blasse, and A. Bril, J. Chem. Phys., 47 (1967) 5139.

[48] T. Hoshina, J. Phys. Soc. Japan., 48 (1980) 1261.

[49] P. Dorenbos, Phys. Rev. B, 62 (2000) 15640.

[50] L. Guerbous, and O. Krachni, J. Modern. Opt., 53 (2006) 2043.

[51] A. H. Krumpel, E. van der Kolk, D. Zeelenberg, A. J. J. Bos, K. W. Krämer, and P. Dorenbos, J. Appl. Phys., 104 (2008) 073505.

[52] N. V. Skorodumova, R. Ahuja, S. I. Simak, I. A. Abrikosov, B. Johansson, and B. I. Lundqvist, Phys. Rev. B, 64 (2001) 115108.

[53] P. J. Hay, R. L. Martin, J. Uddin, and G. E. Scuseria, J. Chem. Phys., 125 (2006) 034712.

[54] B. D. Draeger, and G. P. Summers, Phys. Rev. B, 19 (1979) 1172.

[55] J. M. Costantini, G. Lelong, M. Guillaumet, W. J. Weber, S. Takaki, and K. Yasuda, J. Phys.: Condens. Matter, 28 (2016) 325901.

[56] D. Lesueur, Philos. Mag. A 44 (1981) 905.

[57] K. Yasunaga, K. Yasuda, S. Matsumura, and T. Sonoda, Nucl. Instr. and Meth. B, 266 (2008) 2877.

[58] A. Guglielmetti, A. Chartier, L. van Brutzel, J.-P. Crocombette, K. Yasuda, C. Meis, and S. Matsumura, Nucl. Instr. and Meth. B, 266 (2008) 5120.

[59] H. Y. Xiao, Y. Zhang, and W. J. Weber, Phys. Rev. B, 86, 054109 (2012)

[60] G. F. Imbusch, W. M. Yen, A. L. Schawlow, G. E. Devlin, and J. P. Remeika, 136 (1964) A 481.

[61] T. Sato, Y. Iwamoto, S. Hashimoto, T. Ogawa, T. Furuta, S.Abe, T. Kai, P-E Tsai, N. Matsuda, H. Iwase, N. Shigyo, L. Sihver, and K. Niita, Journal of Nuclear Science and Technology (2018), https://phits.jaea.go.jp

[62] I. Plante, and F. A. Cucinotta, New J. of Phys., 10 (2008) 125020

[63] T. Liamsuwan, and H. Nikjoo, Phys. Med. Biol., 58 (2013) 673.

[64] R. C. Alig, and S. Bloom, Phys. Rev. Lett., 35 (1975) 1522.

[65] J. Sempau, J. M. Fernandez-Varea, E. Acosta, and F. Salvat, Nucl. Instr. and Meth. B, 207 (2003) 107.

[66] S. Agostinelli, J. Allison, K. Amako, J. Apostolakis, H. Araujo, P. Arce, M. Asai, D. Axen, S. Banerjee, G. Barrand, F. Behner, L. Bellagamba, J. Boudreau, L. Broglia, A. Brunengo, H. Burkhardt, S. Chauvie, J. Chuma, R. Chytracek, G. Cooperman, G. Cosmo, P. Degtyarenko, A. Dell'Acqua, G. Depaola, D. Dietrich, R. Enami, A. Feliciello, C. Ferguson, H. Fesefeldt, G. Folger, F. Foppiano, A. Forti, S. Garelli, S. Giani, R. Giannitrapani, D. Gibin, J.J. Gómez Cadenas, I. González, G. Gracia Abril, G. Greeniaus, W. Greiner, V. Grichine, A. Grossheim, S. Guatelli, P. Gumplinger, R. Hamatsu, K. Hashimoto, H. Hasui, A. Heikkinen, A. Howard, V. Ivanchenko, A. Johnson, F.W. Jones, J. Kallenbach, N. Kanaya, M. Kawabata, Y. Kawabata, M. Kawaguti, S. Kelner, P. Kent, A. Kimura, T. Kodama, R. Kokoulin, M. Kossov, H. Kurashige, E. Lamanna, T. Lampén, V. Lara, V. Lefebure, F. Lei, M. Liendl, W. Lockman, F. Longo, S. Magni, M. Maire, E. Medernach, K. Minamimoto, P. Mora de Freitas, Y. Morita, K. Murakami, M. Nagamatu, R. Nartallo, P. Nieminen, T. Nishimura, K. Ohtsubo, M. Okamura, S. O'Neale, Y. Oohata, K. Paech, J. Perl, A. Pfeiffer, M.G. Pia, F. Ranjard, A. Rybin, S. Sadilov, E. Di Salvo, G. Santin, T. Sasaki, N. Savvas, Y. Sawada, S. Scherer, S. Sei, V. Sirotenko, D. Smith, N. Starkov, H. Stoecker, J. Sulkimo, M. Takahata, S. Tanaka, E. Tcherniaev, E. Safai Tehrani, M. Tropeano, P.

Truscott, H. Uno, L. Urban, P. Urban, M. Verderi, A. Walkden, W. Wander, H. Weber, J.P. Wellisch, T. Wenaus, D.C. Williams, D. Wright, T. Yamada, H. Yoshida, D. Zschiesche, “Geant4—a simulation toolkit”, Nucl. Instr. and Meth. A, 506 (2003) 250.

[67] F. Salvat, "*Penelope - a Code System for Monte Carlo Simulation of Electron and Photon Transport. Technical Report*”, Workshop Proceedings Issy-les-Moulineaux, France; AEN-NEA, 5-7 November 2001.

http://geant4-userdoc.web.cern.ch/geant4-userdoc/UsersGuides/PhysicsReferenceManual/html/electromagnetic/introduction/penelope.html

[68] J. Apostolakis et al. "*Geant4: Low Energy Electromagnetic Models for Electrons and Photons*”, CERN-OPEN-99-034(1999), INFN/AE-99/18.

[69] S. M. Seltzer S. T. Perkins, and D. E. Cullen. “*Tables and Graphs of Electron-interaction Cross-sections from 10 eV to 100 GeV Derived from the LLNL Evaluated Electron Data Library (EEDL), Z = 1 - 100*”, Technical Report UCRL-50400, Vol.31, Lawrence Livermore National Laboratory, (1989).

[70] F. Blanco, and F. Arqueros, Phys. Lett., A345 (2016) 355.

[71] L. A. J. Garvie, and P. R. Buseck, J. Phys. Chem. Solids, 60 (1999) 1943.

Table I: Characteristics of electron irradiations of CeO_2 (mass density = 7.215 g cm^{-3}), computed with the ESTAR code [24] for different primary electron energies (E) and mean ionization energy I = 407.6 eV: CSDA range, and total inelastic stopping power ($(-dE/dx)_{inel}$).

E (keV)	20	400	600	800	1,000	1,250
Range (µm)	2.3	289	500	720	943	1,221
$(-dE/dx)_{inel}$ (MeV μm^{-1})	$52x10^{-4}$	$9.9x10^{-4}$	$9.2x10^{-4}$	$9.0x10^{-4}$	$9.0x10^{-4}$	$9.1x10^{-4}$

Table II: CL band characteristics and defect assignments for the CeO_2 polycrystalline sample.

	Band center (eV)	FWHM (eV)	Defect
HVEM (300 K)	4.2	1.0	F^+ center
	2.8	0.4	Ce^{3+} (Ce_I)
	2.3	0.6	Ce^{3+} (Ce_{II})
	1.7	0.4	Impurity
HVEM (100 K)	4.2	1.0	F^+ center
	2.9	1	Ce^{3+} (Ce_I)
	2.0	0.5	Ce^{3+} (Ce_{II})
	1.7	0.4	Impurity
SEM (300 K)	2.8	0.7	Ce^{3+} (Ce_I)
	2.4	0.6	Ce^{3+} (Ce_{II})

Table III: Expected evolutions of the various cross sections (see text) for increasing electron energy (E ↑) and decreasing temperature (T ↓), and combined effects (E ↑ X T ↓):

	σ_i	σ_t	σ_e	σ_r	σ_{CL}	σ_d
E ↑	–	–	↓	↓	↓	↑
T ↓	–	↓	–	↑	Max	–
E ↑ X T ↓	–	↓	↓	↑	Max / ↓	↑

Table IV: Total integrated electron production cross section ($\sigma_{i,tot}$) computed with various codes.

E (keV)	PHITS [59] $\sigma_{i,tot}$ (b)	PENELOPE [65] $\sigma_{i,tot}$ (b)	LIVERMORE [64] $\sigma_{i,tot}$ (b)	EMX [66] $\sigma_{i,tot}$ (b)
400	68,891	74,914	65,235	63,324
1,250	51,748	60,841	54,723	47,789

Table V: Fitting parameters for the electron-energy dependence of CL bands of CeO_2.

Single crystal band centers (eV)	Defect	E_0 (keV) (300 K)	α (300 K)	β (300 K)	E_0 (keV) (200 K)	α (200 K)	β (200 K)	E_0 (keV) (100 K)	α (100 K)	β (100 K)
2.4-2.6	Ce^{3+} (Ce_{II})	396	1.11	0.39	250	0	0.34	340	0.03	0.43
2.8-3.0	Ce^{3+} (Ce_{I})	396	1.39	0.39	250	0	0.34	371	0	0.45
4.2	F^+ center	399	2.20	0.37	287	0	0.36	355	0	0.36
Polycrystal band centers (eV)										
2.0-2.3	Ce^{3+} (Ce_{II})	398	1.57	0.25	375	1.23	0.27	387	1.22	0.28
2.8-2.9	Ce^{3+} (Ce_{I})	398	1.41	0.25	375	0.96	0.27	397	1.1	0.28
4.2	F^+ center	388	0.61	0.37	385	0.67	0.38	396	0.41	0.32

Figure 1: CL spectra at ~300 K of the CeO_2 single crystal and polycrystalline sample for 20-keV electron excitation. Dashed lines are the fitted spectra and dotted lines are the Gaussian curves used for least-square fits.

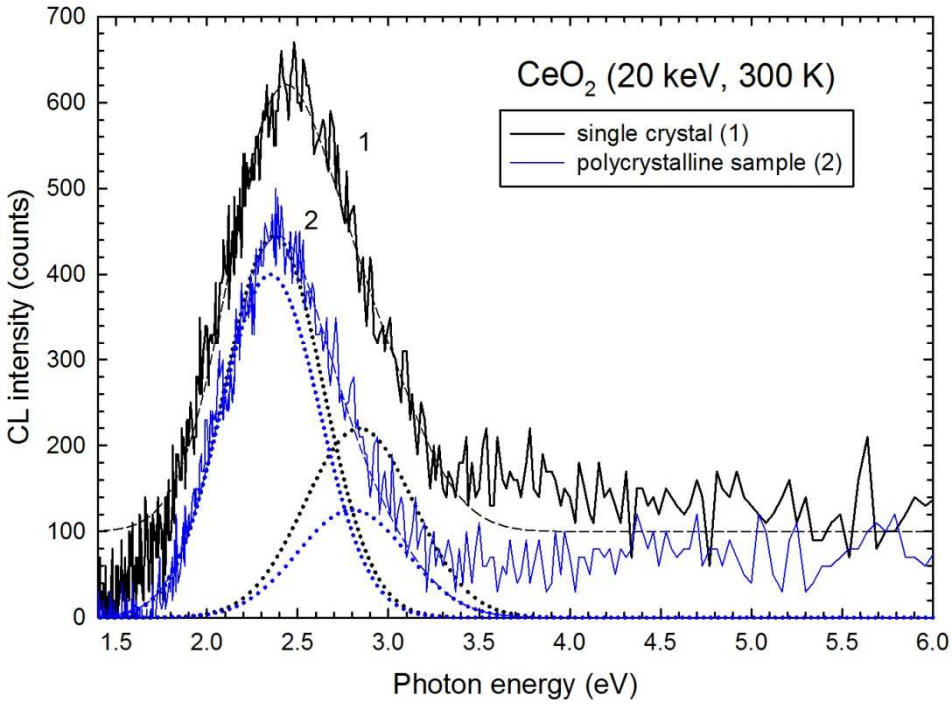

Figure 2: CL spectra at ~300 K of the CeO_2 single crystal (a) and polycrystalline (b) sample for electrons of variable energy at fluences of $1.1x10^{24}$ m^{-2} and $5.7x10^{23}$ m^{-2}, respectively. CL spectra at ~100 K of the CeO_2 single crystal (c) and polycrystalline sample (d) recorded in similar conditions. Dashed lines are the fitted spectra and dotted lines are the Gaussian curves used for least-square fits.

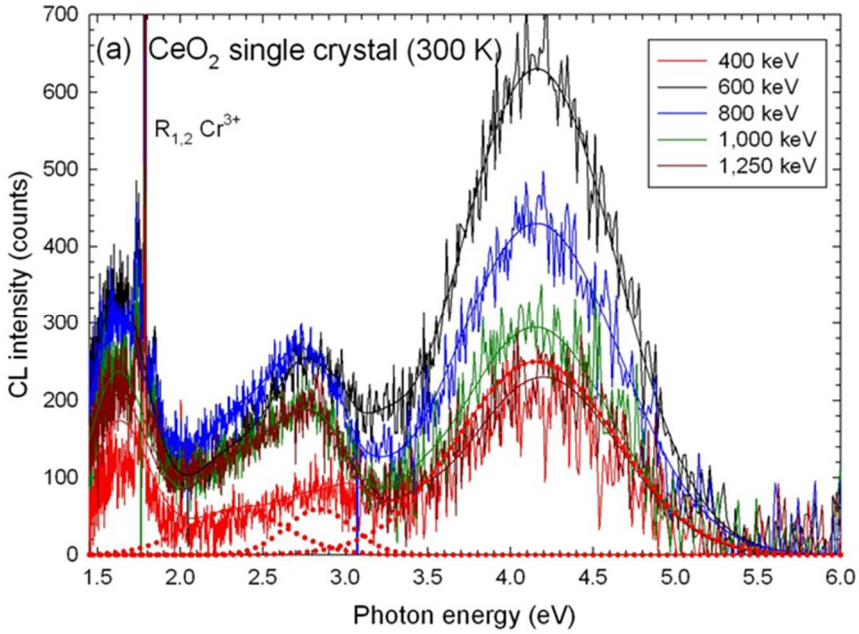

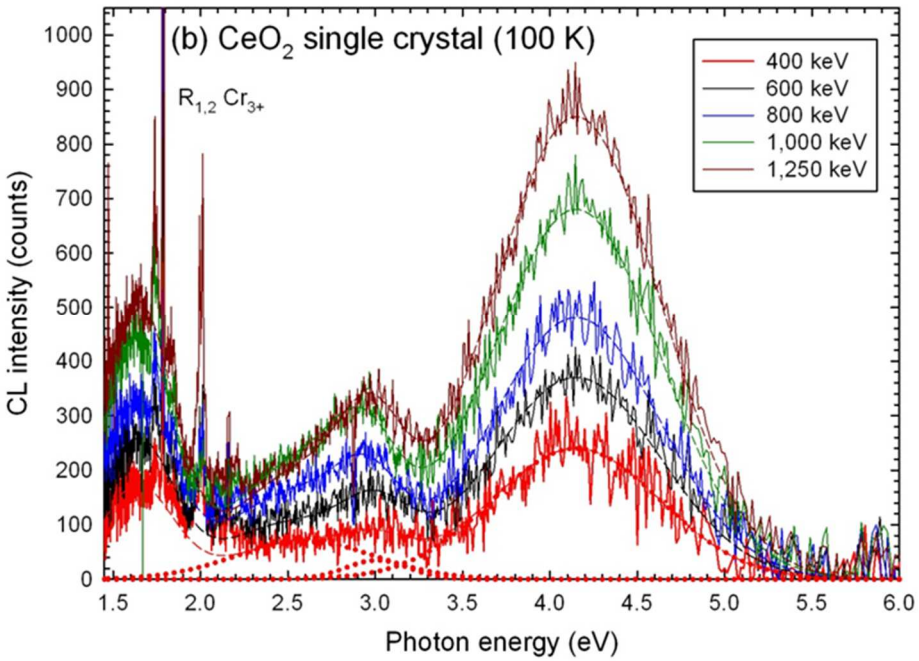

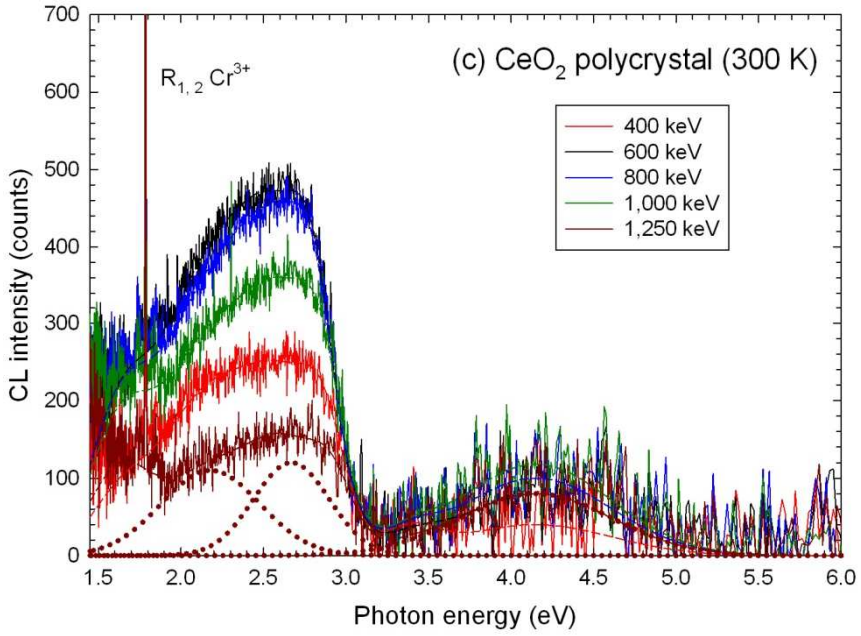
(c) CeO2 polycrystal (300 K)
R1, 2 Cr3+
400 keV
600 keV
800 keV
1,000 keV
1,250 keV
CL intensity (counts)
Photon energy (eV)
0
100
200
300
400
500
600
700
1.5
2.0
2.5
3.0
3.5
4.0
4.5
5.0
5.5
6.0

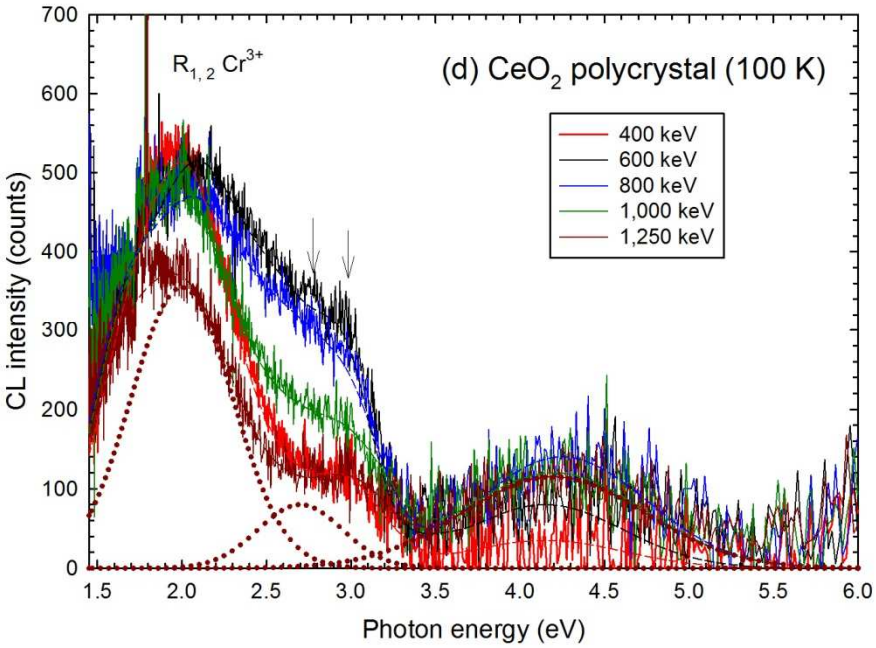
(d) CeO2 polycrystal (100 K)
R1, 2 Cr3+
400 keV
600 keV
800 keV
1,000 keV
1,250 keV
CL intensity (counts)
Photon energy (eV)
0
100
200
300
400
500
600
700
1.5
2.0
2.5
3.0
3.5
4.0
4.5
5.0
5.5
6.0

Figure 3: CL integrated intensities of the CL bands at ~300 K (a), 200 K (b), and 100 K (c) versus electron energy for the CeO_2 single crystal (full symbols) and polycrystalline sample (open symbols). Each set of data was recorded for a similar flux and fluence (Figs. 2a-d). Solid and dashed lines are least-square fits with Eq. (1) for the single crystal and polycrystalline sample, respectively. The dotted line is a linear regression for the single crystal data (c).

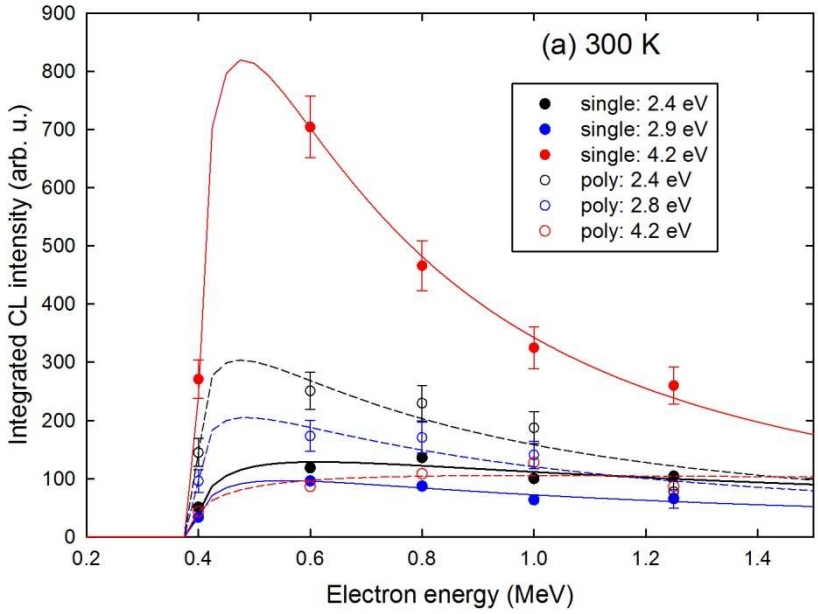

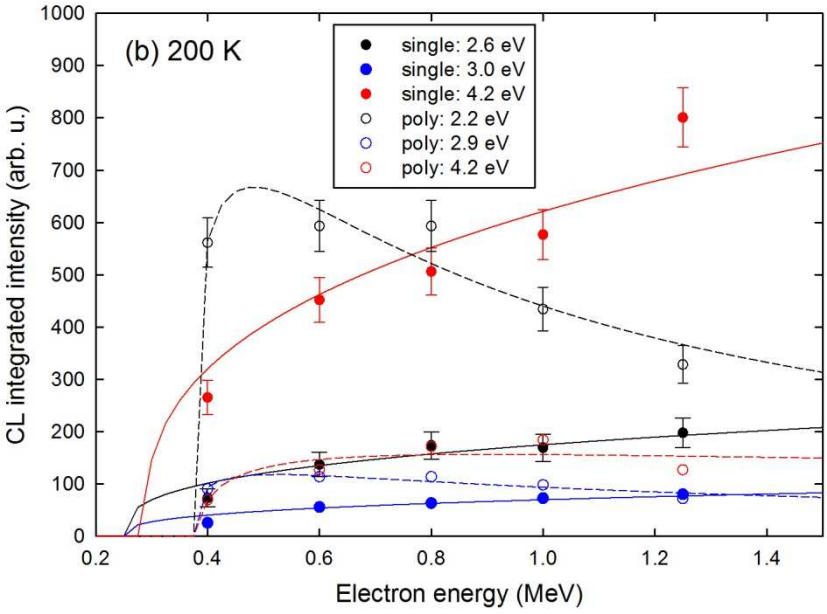

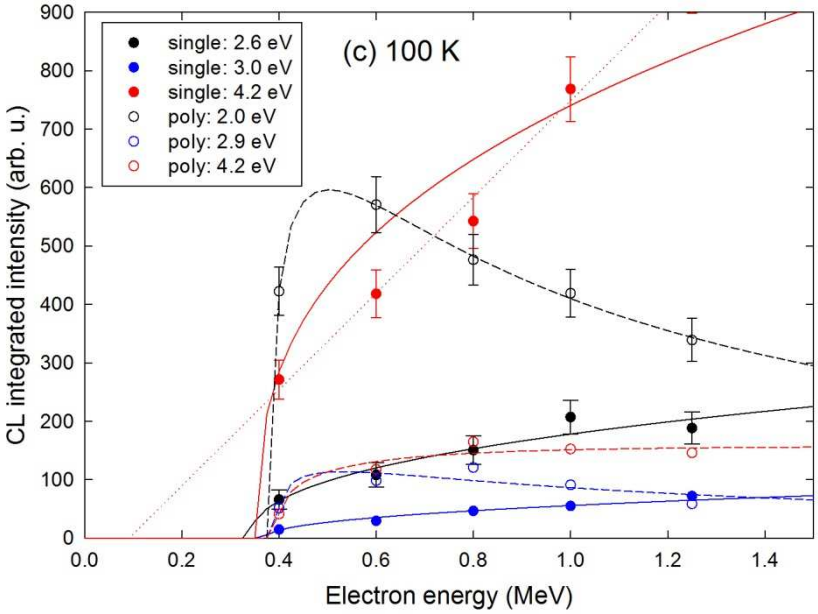
single: 2.6 eV
single: 3.0 eV
single: 4.2 eV
poly: 2.0 eV
poly: 2.9 eV
poly: 4.2 eV
(c) 100 K
CL integrated intensity (arb. u.)
Electron energy (MeV)
0
100
200
300
400
500
600
700
800
900
0.0
0.2
0.4
0.6
0.8
1.0
1.2
1.4

Figure 4: a) Schematic representation of different electronic configuration of a neutral oxygen vacancy in CeO_2; b) Sketch of electronic levels in the band gap of CeO_2 possessing oxygen vacancies; c) Schematic configuration coordinate representation of the F^+ emission. The site of the unpaired electron is represented in red.

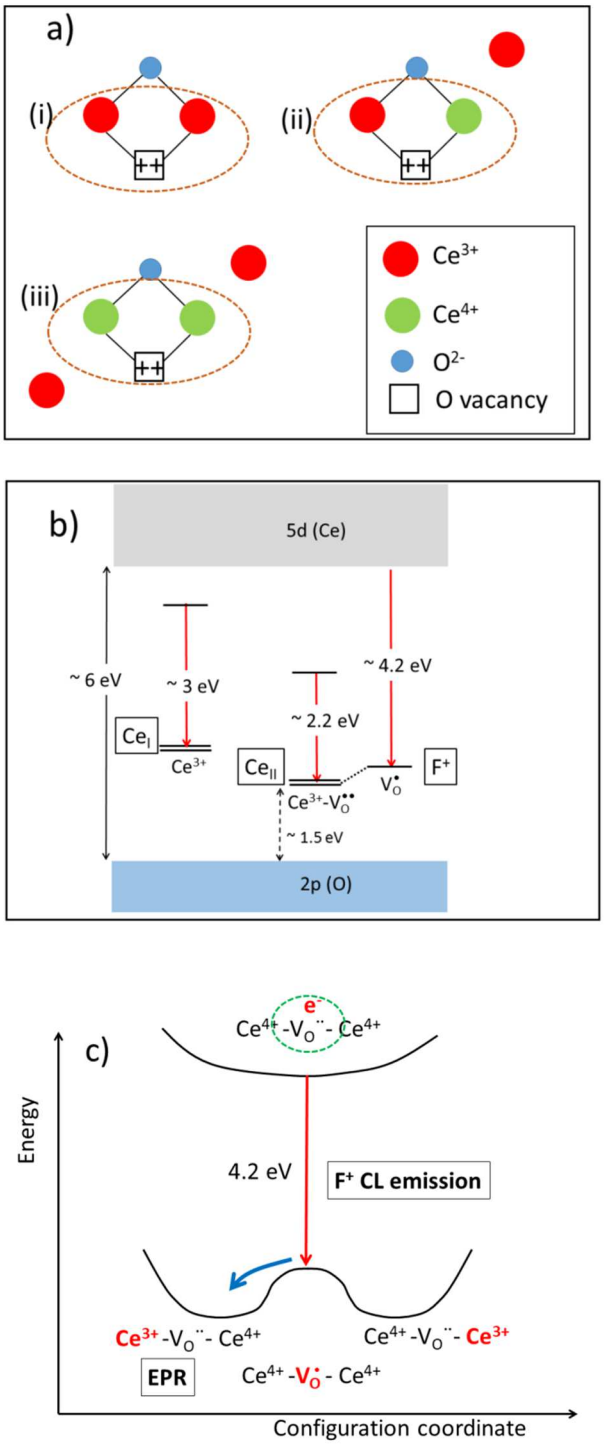

Figure 5: Assignment of CL bands at ~300 K of the CeO_2 single crystal for 1,250-keV electron excitation. Dotted lines are the Gaussian curves used for fits of spectra and the dashed line is the fitted spectrum.

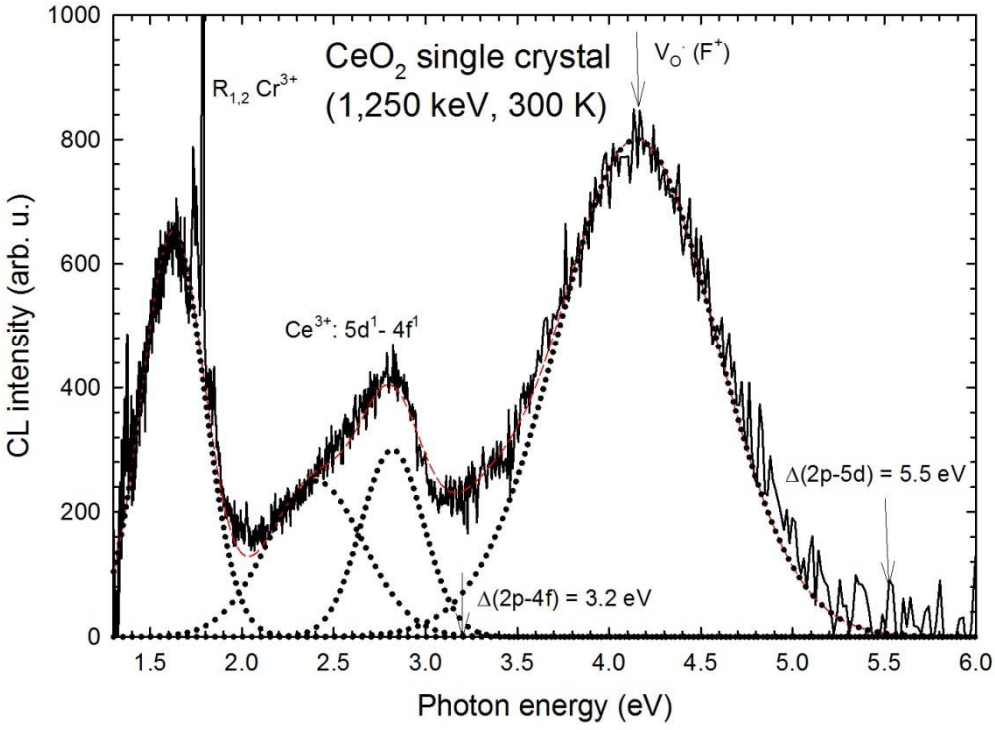

Figure 6: Secondary-electron energy spectra generated by primary electrons of 400 keV, 800 keV, and 1,250 keV on Ce and O atoms), in the forward direction ($0° \leq \theta \leq 18°$) computed with the PHITS code [59]: double differential electron-electron collision cross section ($d^2\sigma_i/dE_s d\Omega$) per secondary electron energy step (E_s) and solid angle (Ω) versus E_s. The vertical dotted lines represents the maximum energy of secondary electrons (E_{cut}) confined inside the 150-µm or 0.5-mm thick CeO_2 targets. Solid curves are the Ce data, and dashed curves are the O data.

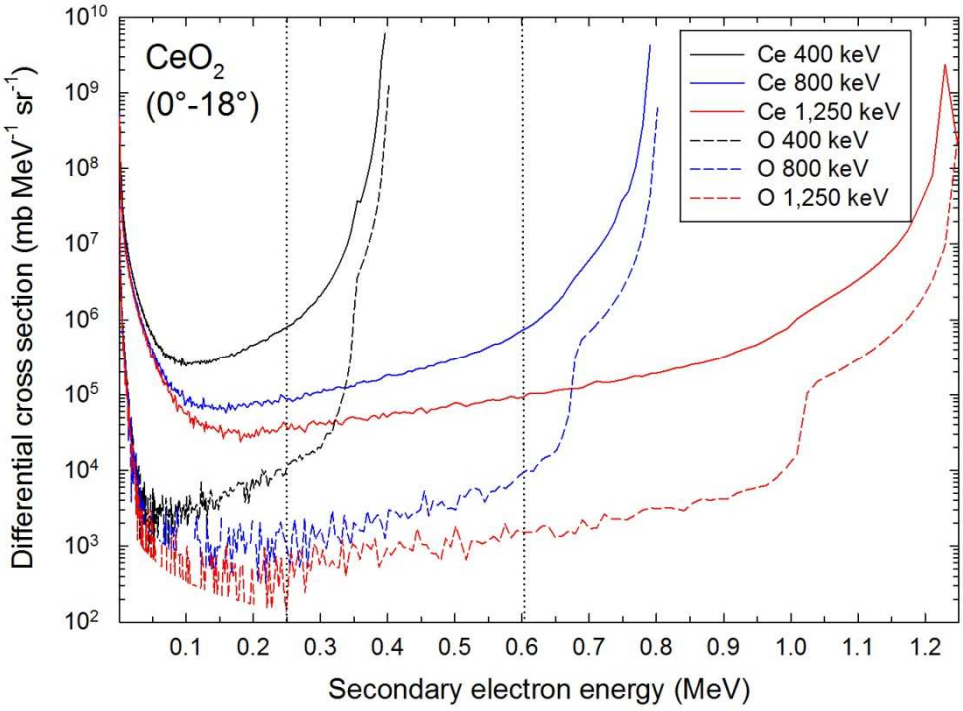

Figure 7: PHITS simulations [59] of the total displacement per atom (dpa) and the number of secondary electrons per primary electron down-scattered to 1 keV inside a 150-µm thick ceria sample versus primary electron energy (E). The solid line is a guide to the eyes and the dashed line is a linear regression.

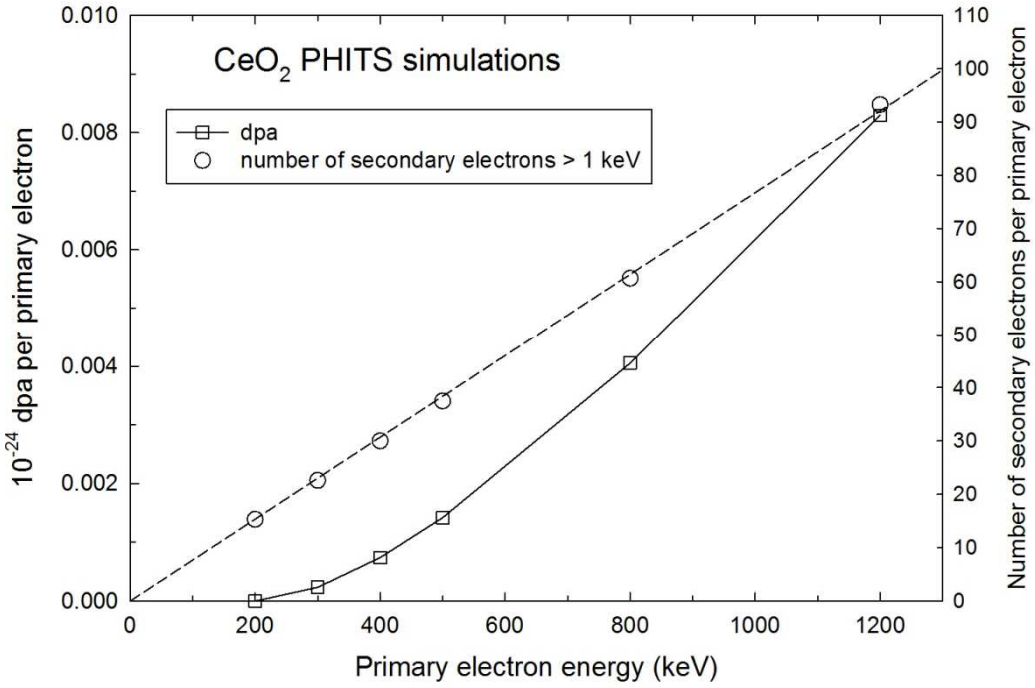

Figure 8: Differential ionization cross section ($d\sigma_i/d\theta$) for the Ce atoms as a function of scattering angle (θ) for primary electron energies of 400 keV (solid lines) and 1,250 keV (dashed lines) computed with the PHITS code [59] and various computer codes [63-66].